CrystEngComm

ROYAL SOCIETY OF CHEMISTRY

PAPER

View Article Online
View Journal | View Issue

Cite this: *CrystEngComm*, 2025, **27**, 7358

Structural chemistry and environment-dependent fluorescence of a tetratopic pyrrolo[3,2-*b*]pyrrole ligand

Corey L. Brown,†[a] Scarlett H. Elliott,†[a] Sian E. Woodfine[b] and Chris S. Hawes *[a]

Received 25th September 2025,
Accepted 26th October 2025

DOI: 10.1039/d5ce00926j

rsc.li/crystengcomm

Here we report a new tetratopic carboxylic acid ligand H_4**L1** containing a fluorescent pyrrolo[3,2-*b*]pyrrole core, and examine its structural chemistry in two solvated forms with amide solvents and a porous strontium(II) MOF. The two solvates H_4**L1**·2DMF and H_4**L1**·4DMA exhibit similar hydrogen bonding characteristics at the *N*-aryl position, but are differentiated by the hydrogen bonding behaviour of the *C*-aryl position; while the DMF solvate forms a one-dimensional chain *via* carboxylic acid dimers, the DMA solvate is fully enclosed by solvent molecules occupying all hydrogen bonding sites. The tendency for the electron-rich core to avoid close π···π interactions in these solvates is further evident in the structure of poly-[Sr_2(**L1**)(DMF)$_2$(OH_2)]·DMF·H_2O **1**, a 3-dimensional rod-packed MOF with narrow linear solvent channels. Exchange of the lattice solvent with methanol, with retention of single crystallinity, gives a framework which can be readily desolvated, and exhibits a maximum CO_2 uptake of 8 wt% at 283 K and 1 atm. The ligand is strongly fluorescent in DMSO in its protonated and deprotonated forms and exhibits characteristic solvatochromism, which is pronounced in solution and remains evident, to a lesser degree, in the fluorescent MOF **1**.

Introduction

Designing coordination polymers and metal–organic frameworks (MOFs) exhibiting easily-detectable physical responses to chemical stimuli remains an important growth area in crystal engineering.[1] Taking advantage of confinement effects governing the interactions between small molecules and micropore environments,[2] opportunities exist for a wide range of detection and reporting mechanisms. Various metal-centred reporting mechanisms have been explored, such as MOF systems which undergo a change in magnetic susceptibility or metal-centred phosphorescence upon guest uptake.[3] However, a much wider scope of possible chemical sensing and reporting mechanisms can be embedded within the organic components of MOFs, thanks to the ever-expanding pool of ligand functionalities which are continually being developed.[4] To this end, MOF-based sensors incorporating anion receptors,[5] AIEgens,[6] additional metal binding sites,[7] or on/off fluorescent sensing tags have shown important progress in recent years.[8] However, while on/off fluorescent sensors are useful for qualitative detection of small molecule analytes,[9] sensors whose output is quantifiable ratiometrically or by emission colour (rather than absolute intensity) are more practically useful in the presence of absorbing or quenching species in real-world mixtures.[10]

Since the early reports of tetraaryl-pyrrolo[3,2-*b*]pyrrole (TAPP) fluorophores by Gryko and co-workers,[11] there has been widespread interest in their electronic behaviour. When substituted with strongly electron withdrawing functionality at the *C*-aryl position,[12] TAPP fluorophores can exhibit record levels of solvatochromism in their emission spectra. A series of subsequent studies has proven the synthetic versatility and potential for wider functionalisation of these species.[13] A range of higher fused systems derived from the pyrrolo[3,2-*b*]pyrrole core have also now been reported and spectroscopically investigated.[14] The good functional group tolerance for the condensation reaction typically used to form the fused core also makes this scaffold attractive for structural chemistry and crystal engineering. Since the first crystallographically-characterised MOF containing a TAPP fluorophore in 2018,[15] several studies have reported the synthesis of MOFs and coordination polymers from TAPP-based ligands, mostly employing carboxylate functional groups.[16] From a crystal engineering perspective, TAPP systems tend to exhibit packing modes with limited involvement of the pyrrolic core by virtue of their centrosymmetry, non-coplanar aryl arms and electron rich cores. This distinguishes them from strongly aggregating dipolar fluorophores like 1,8-naphthalimides,[17] and allows

[a] *School of Chemical and Physical Sciences, Keele University, Keele ST5 5BG, UK. E-mail: c.s.hawes@keele.ac.uk*
[b] *Faculty of Natural Sciences, Keele University, Keele ST5 5BG, UK*
† These authors contributed equally.

for the design of MOFs, and potentially other metallosupramolecular systems,[18] allowing access of small molecules to the active fluorescent core.

In terms of utility for responsive fluorescent systems, Gryko and co-workers have shown that the nature of the *C*-aryl substituent is mostly responsible for the fluorescent properties of the TAPP fluorophore.[19] To date, the studies concerned with optical emission in MOFs containing TAPP fluorophores have often focused on coordination through this position. In our previous work,[15] we reported fluorescent silver(I) and zinc(II) MOFs based on TAPP fluorophores, which were emissive when coordination occurred through the *C*-aryl positions only. However, installing an *N*-phenylimidazole linker at the *N*-aryl position of the pyrrolopyrrole core gave a tetratopic ligand which was emissive in its free form but non-emissive when coordinated to cadmium(II). We tentatively ascribed the fluorescence quenching in this system to a combination of reduced electron donor capability and introduction of further non-radiative decay pathways, both arising from conjugation of a heavy cation to the pyrrolic nitrogen atoms. Based on these previous findings, we envisaged a modified tetratopic TAPP ligand where the conjugation between the metal binding site and the pyrrolic nitrogen was disrupted. Herein we report the synthesis and spectroscopic characterisation of a new tetratopic TAPP ligand **H_4L1** where the *C*-aryl binding site is disrupted from the pyrrolic core by a methylene linker, its structure and interactions in the crystalline phase, and its incorporation into a fluorescent strontium(II) MOF.

Results and discussion

Synthesis and structural characterisation of H_4L1

The ligand **H_4L1** was prepared using the general method reported by Gryko,[11] using 4-aminophenylacetic acid, 4-formylbenzoic acid and 2,3-butanedione as reagents in acetic acid with a *p*-toluenesulfonic acid catalyst. The product was isolated as a yellow powder with low solubility (Scheme 1).

During our initial screening attempts to crystallise coordination compounds containing **H_4L1** or its anions, we found (relating to its low solubility) a strong tendency for preferential crystallisation of the free ligand as one of two solvates in amide solvents, shown in Fig. 1. Both solvates adopt the triclinic crystal system, with different lattice

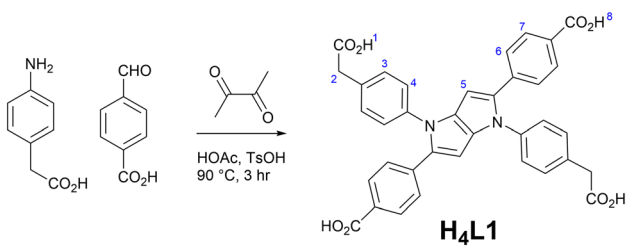

Scheme 1 Synthesis and structure of H_4L1, with numbering scheme for ^{1}H NMR shown in blue.

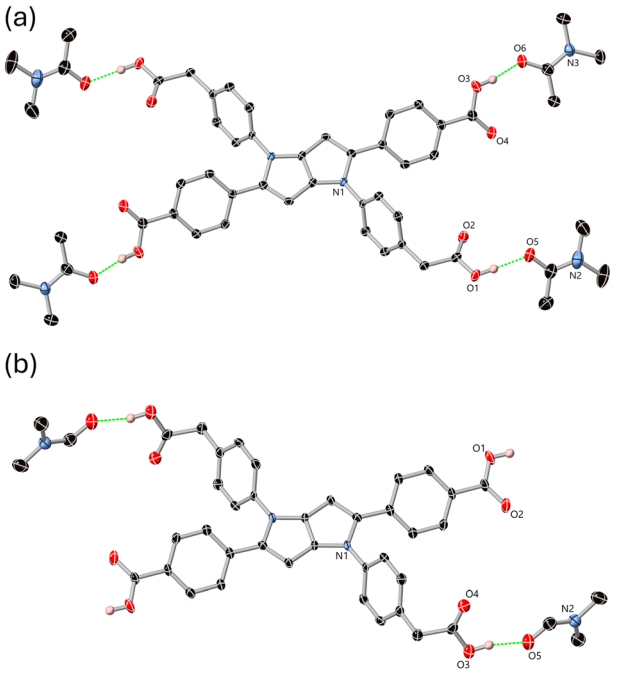

Fig. 1 The structures of (a) H_4L1·4DMA and (b) H_4L1·2DMF with labelling schemes for unique heteroatoms. Hydrogen atoms not involved in hydrogen bonding are omitted for clarity. Ellipsoids are rendered at the 50% probability level.

parameters commensurate with distinct packing modes and unit cell contents. Each of the two phases crystallises independently; crystallisation of the ligand from *N*,*N*-dimethylacetamide gives **H_4L1**·4DMA exclusively, and crystallisation from a 2 : 1 mixture of *N*,*N*-dimethylformamide and water gives only **H_4L1**·2DMF. Rietveld refinement of the X-ray powder diffraction patterns confirmed no additional **H_4L1**-containing phases were present in any significant quantity, and that the unit cell parameters experienced little change at room temperature compared to those at 150 K from the single-crystal datasets (SI, Table S2).

In the DMA solvate, the asymmetric unit contains one half of the centrosymmetric **H_4L1** molecule and two DMA molecules, each occupying hydrogen bonding positions with the two unique carboxylic acid groups. As expected for TAPP derivatives, all four aryl rings are twisted with respect to the central pyrrolopyrrole core, with the *C* substituents adopting a smaller interplanar angle of 27.1° relative to the core while the *N* substituents take on a relative twist angle of 66.5°. The four carboxylic acid groups are capped by hydrogen bonding interactions to the oxygen atom of the dimethylacetamide solvent species, shown in Fig. 2. Two unique interactions are evident, with essentially equivalent donor···acceptor distances of 2.582(3) and 2.591(3) Å and D–H···A angles of 169 and 173° for the *C*- and *N*-aryl groups, respectively.

When crystallised from DMF, the predominant polymorph is the disolvate **H_4L1**·2DMF, adopting a slightly smaller unit cell (SI, Tables S1/S2). The **H_4L1** species adopts a very similar conformation to that seen in the tetrasolvate above, with an

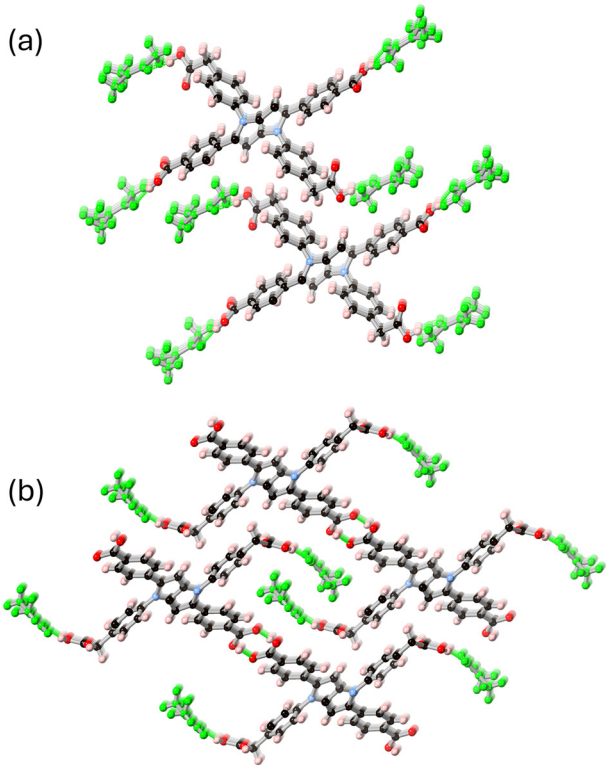

Fig. 2 The extended structures of (a) H_4**L1**·4DMA and (b) H_4**L1**·2DMF showing their predominant interaction with solvent molecules (coloured green) through hydrogen bonding, where the DMF solvate (b) also exhibits a carboxylic acid dimer-type hydrogen bonding contact with another equivalent molecule.

identical interplanar angle of 27.1° for the *C*-aryl group, and a slightly less twisted 59.7° interplanar angle for the *N*-aryl substituent. The carboxylic acid of the *N*-aryl substituent engages in hydrogen bonding with the oxygen atom of the lattice DMF molecule with similar parameters to that observed in the tetrasolvate, with a donor···acceptor distance 2.594(3) Å and D–H···A angle of 153°. In contrast to the tetrasovlate however, in H_4**L1**·2DMF the *N*-aryl carboxylic acid forms a centrosymmetric $R_2^2(6)$ hydrogen bonded dimer with the adjacent molecule with donor···acceptor distance 2.623(3) Å and D–H···A angle 173°. Expansion through this contact forms a one-dimensional hydrogen bonded chain in the [2,0,1] direction.

Beyond hydrogen bonding, H_4**L1**·2DMF has a similar capacity for intermolecular interaction to the tetrasolvate. Notably, neither solvate exhibits any significant (face to face) π···π interactions, despite the large aromatic surface. This is evident in the Hirshfeld surfaces of the solvates (SI, Fig. S2–S5); fingerprint plots of each show minimal features ascribed to C···C contacts from π···π interactions, where the surface features are instead dominated by the strong and directional O···H contacts and more diffuse C–H···C contacts. Indeed, the closest association between molecules of H_4**L1** in both solvates perpendicular to the hydrogen bonding axes is the offset slipped stack where the C–H edges from the *N*-aryl rings are oriented towards the

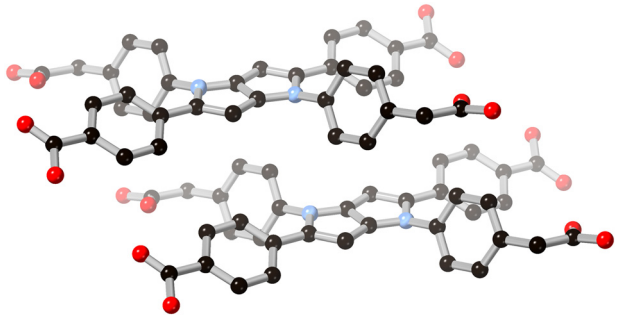

Fig. 3 The offset stacking mode of adjacent molecules of H_4**L1** within the structures of both solvates, where the primary interaction mode is edge-to-face rather than face-to-face contacts between aromatic groups. Hydrogen atoms are omitted for clarity.

pyrrole core of adjacent molecules, shown in Fig. 3. This mode of intermolecular interaction is consistent with both the centrosymmetric character of the π surface and the steric influence of the four non-coplanar aryl substituents hindering the close approach of the two pyrrolic cores. As a result, the pyrrolopyrrole centroids are separated by a minimum of 5.95–6.02 Å in both structures.

Synthesis and structural characterisation of poly-[Sr_2(L1)(DMF)$_2$(OH$_2$)]·DMF·H_2O 1

Having established the structural behaviour of the neutral forms of H_4**L1**, we went on to examine its coordination tendencies and capacity for forming polymeric structures. To do so we focused on closed-shell oxophilic cations, to avoid the likely fluorescence quenching pathways which are prevalent in many transition metal systems.[20] Combining H_4**L1** with strontium nitrate tetrahydrate in a DMF : H_2O mixture and heating at 100 °C for 48 hours gave orange block crystals in 58% yield. Analysis by single crystal X-ray diffraction provided a structural model in the triclinic space group $P\bar{1}$. The asymmetric unit contains two unique strontium sites, two halves of independent $L1^{4-}$ anions, an aqua ligand and two coordinated DMF species, and lattice DMF and water molecules. While crystallographic disorder is evident on the lattice solvent and coordinated DMF species, the main residue is well-ordered. The ligand and metal environments in complex **1** are shown in Fig. 4.

Both ligand residues in the structure of **1** adopt high-connectivity bridging modes involving all four carboxylate groups. The first residue (O1–O4) bridges eight strontium ions with the *N*-aryl carboxylates purely chelating and the *C*-aryl carboxylates bridging three strontium positions each in a μ_3-κO:κO,O′:κO′ mode. The second residue O5–O8 bridges ten strontium ions, with the *N*-aryl carboxylates adopting the same μ_3 bridging mode previously described, while the *C*-aryl carboxylates bridge two strontium ions in a μ_2-κO:κO,O′ mode (Fig. 4). Both strontium ions adopt 8-coordinate dodecahedral geometries, with the coordination spheres completed by one DMF and one aqua ligand (Sr1) or

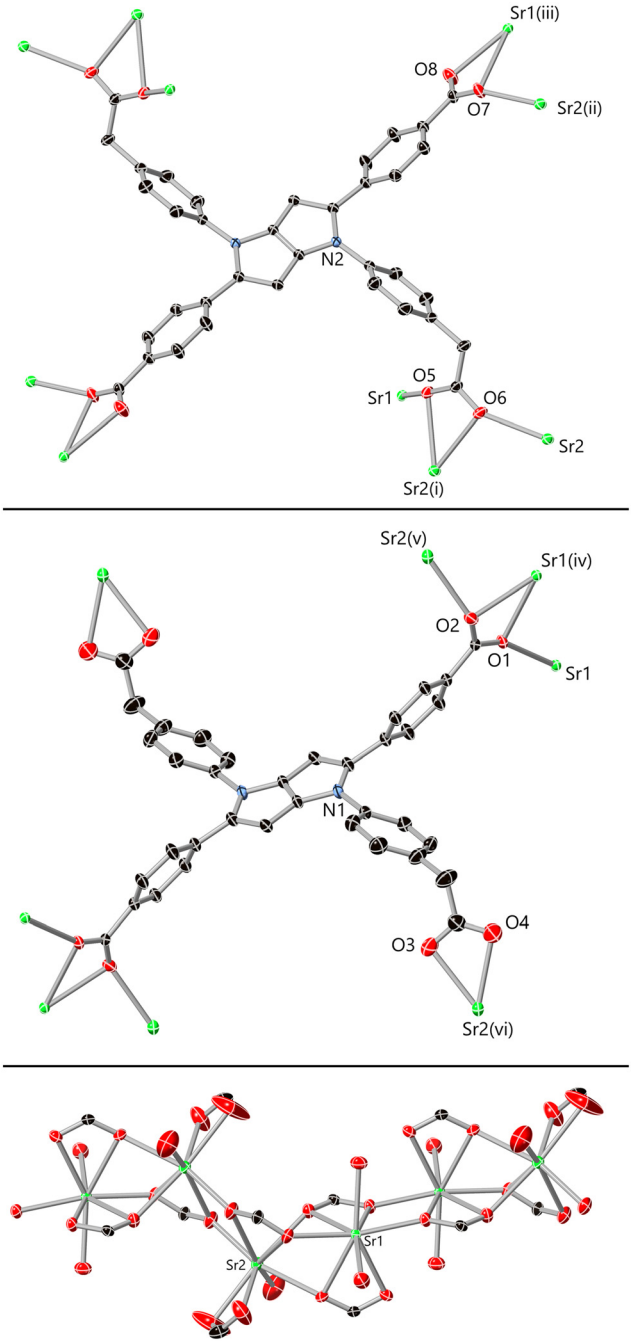

Fig. 4 The ligand and metal environments in the structure of complex **1**, showing the bridging modes of the ligands (Top/Middle) and the metal carboxylates chains formed by the two unique strontium ions (Bottom). Labelling schemes are shown for unique heteroatoms and hydrogen atoms and solvent molecules are omitted for clarity. Ellipsoids are rendered at the 50% probability level. Symmetry codes used to generate equivalent atoms: (i) 2 − *x*, 1 − *y*, −*z*; (ii) *x* − 1, +*y*, *z* + 1; (iii) 1 − *x*, 1 − *y*, 1 − *z*; (iv) 1 − *x*, 1 − *y*, −*z*; (v) *x* − 1, +*y*, +*z*; (vi) *x* − 1, +*y*, *z* + 1.

one DMF ligand (Sr2). The **L1** residues adopt slightly more deformed conformations than those observed in the free ligands; the mean interplanar angles from the pyrrolopyrrole cores to the and *C*-aryl substituents are larger than observed in the free ligand structures (55.2° and 39.5°), while the angles involving the *N*-aryl substituent are smaller (49.7° and 39.6°). A notable bend is also evident across the long axis of the molecule, with the (*C*-aryl) carboxylate carbon atom C1 lying 1.9 Å out of the pyrrolopyrrole mean plane; in the two ligand solvates, the equivalent distance does not exceed 0.3 Å.

The carboxylate coordination modes give rise to monoatomic bridges between adjacent strontium ions with interatomic distances of 4.0898(6) Å for Sr1–Sr1′, 3.8220(4) Å for Sr1–Sr2 and 4.1808(5) Å for Sr2–Sr2. These close linkages encourage the formation of polymeric strontium carboxylate chains parallel to the crystallographic *a* axis, each of which is densely interconnected *via* $\mathbf{L1}^{4-}$ anions which bridge between four adjacent rods. A similar tendency for aversion of close contacts between the pyrrolopyrrole cores is observed in these anions, where the primary mode of interaction between adjacent $\mathbf{L1}^{4-}$ units is *via* edge-to-face interactions between the pyrrolopyrrole cores and the peripheral phenyl rings, rather than between the cores themselves (Fig. 5). When viewed parallel to these rod-like secondary building units, the extended structure contains approximately square one-dimensional solvent channels of *ca.* 9 × 8 Å interatomic dimensions, occupied by lattice and coordinating DMF molecules.

Solvent exchange and gas adsorption studies

To probe the internal surfaces of compound **1**, the crystals were immersed in methanol for 48 hours, renewing the supernatant with fresh methanol every 12 hours, to fully exchange the lattice and coordinated DMF. Thermogravimetric analysis revealed a significant change in the volatile fraction of the two materials (SI Fig. S12). The pristine **1** exhibits minimal mass loss below 100 °C followed by a complex multi-step desolvation process initiating at 125 °C with a gentle plateau only being reached at *ca.* 400 °C before the onset of wider decomposition above 500 °C. The

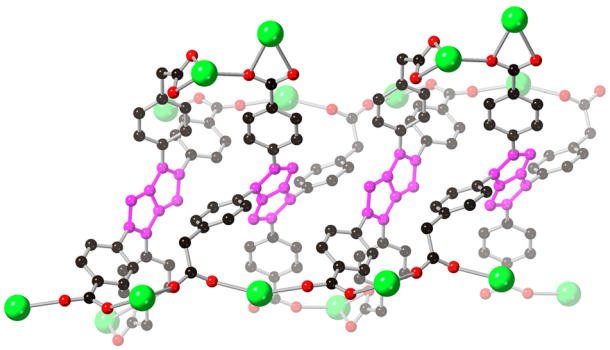

Fig. 5 A stack of four adjacent $\mathbf{L1}^{4-}$ bridging ligands viewed perpendicular to the metal–carboxylate chains. The central pyrrolopyrrole units are highlighted in pink, showing the tendency of these electron rich units to avert direct π···π interactions and instead stack through edge-to-face C–H···π contacts involving the peripheral phenyl rings.

total mass loss at this temperature (22% at 400 °C, *vs.* 24.4% total calculated volatiles) indicates direct thermal desolvation is unlikely to be effective in the pristine sample. In contrast, the methanol-exchanged material begins desolvating near room temperature with a maximum $-dW/dT$ at 100 °C, with a stable plateau above 120 °C until the onset of decomposition above 500 °C. The total mass loss in the methanol exchanged material of *ca.* 15% indicates retention of similar pore volume in the exchanged material.

Surprisingly, despite the significant changes to the volatile component of the pore volume on solvent exchange with methanol, the crystals of **1** visually appeared to retain single crystallinity throughout the solvent exchange process, although they subsequently proved very sensitive to solvent loss on drying in air. Nonetheless, a single crystal of the exchanged compound **1-MeOH** was subjected to analysis by single crystal X-ray diffraction. Although the resolution and intensity of the reflections were somewhat reduced compared to the pristine sample, a suitable structural model could still be obtained. The exchanged material retained the same symmetry and very similar lattice parameters and unit cell volume as the pristine compound at both 150 K and room temperature (Tables S1 and S2, SI), and while the solvated portion of the unit cell was heavily disordered, the main residue essentially remained well-ordered.

The ligand geometries in **1-MeOH** are closely related to those from the pristine compound; the interplanar angles between the pyrrolopyrrole cores and the *N*-aryl substituents of 44.0 and 47.0, and to the *C* aryl substituents of 36.2° and 50.5° all fall within *ca.* 5° of the equivalent metrics from the freshly prepared **1**. The coordination geometries of the strontium ions are likewise essentially unchanged, and the Sr–Sr distances all fall in similar ranges to those observed in the pristine structure. The extended structure retains the size and shape of the solvent channels evident in the parent framework, as shown in Fig. 6. The identity of the coordinating solvent molecules could not be unambiguously determined crystallographically; while the oxygen positions were best modelled as water, most likely these sites are occupied by a disordered mixture of water and methanol species. Two relatively well-ordered lattice methanol molecules and a lattice water molecule were identified in likely hydrogen bonding positions, but the remaining solvated volume (198 $Å^3$, 68 e^- per formula unit) was accounted for with a solvent mask (SI). The total solvent-accessible volume within the structure of **1-MeOH**, including both the localised lattice solvent and the disordered regions, is approximately 32% of the total unit cell volume.

To test the potential for gas uptake within compound **1**, the methanol-exchanged **1-MeOH** was activated under dynamic vacuum at 100 °C for 12 hours, before fully evacuating under a turbomolecular pump at 100 °C for a further 8 hours. The activated sample was then subjected to adsorption of N_2 at 77 K and CO_2 at 283, 293 and 303 K. Unsurprisingly given the narrow solvent channels, we observed minimal adsorption of N_2 within the activated material across the full pressure range 0–0.99 P/P_0 (SI, Fig. S13). Adsorption of CO_2 at 283 K however showed improved performance, where the adsorption curve across the pressure range 0–100 kPa rose to a maximum loading of 45 cc(STP) g^{-1} (8 wt%) at the upper end of the pressure range, shown in Fig. 7. Using the CO_2 adsorption data across the three temperatures measured, the isosteric enthalpy of adsorption across the loading range was estimated using a Virial method. The value obtained by extrapolating to zero loading of −42.5 kJ mol^{-1} is relatively large, and comparable to other small-pore MOFs where a larger fraction of the adsorbate surface is in contact with the concave pore surfaces.[21] Given the high coordination number of the strontium ions and presence of a single continuous desolvation step in the TGA, removal of the aqua ligands in the activation process may unmask sites of higher Lewis acidity within the activated framework. Indeed, the rapid decrease in adsorption enthalpy to −37.5 kJ mol^{-1} at 2 mmol g^{-1} CO_2 loading is also consistent with early filling of stronger binding sites followed by less favourable physisorption on the remaining pore surfaces.

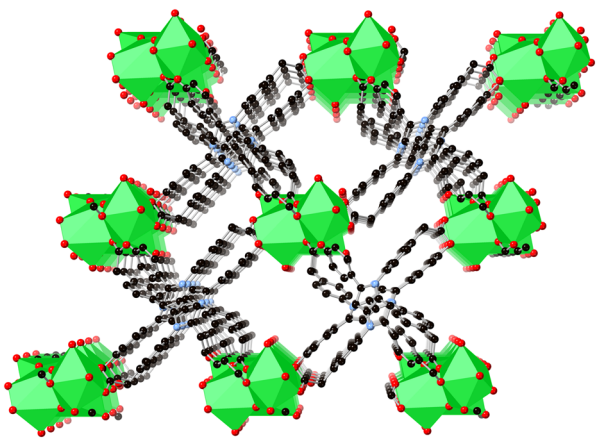

Fig. 6 Extended structure of compound **1-MeOH** with lattice solvent molecules omitted, viewed parallel to the primary solvent channels.

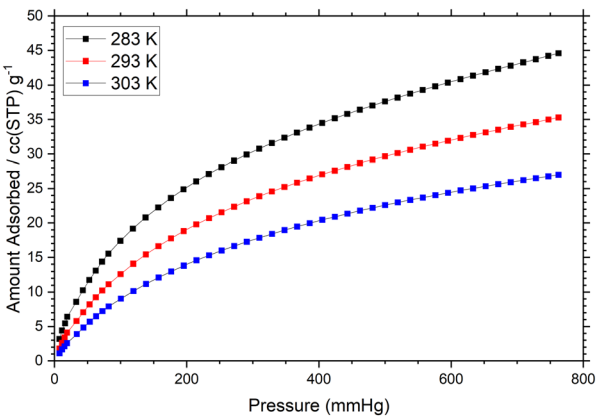

Fig. 7 Adsorption isotherms for CO_2 within the activated **1-MeOH** measured in 10 K increments from 283 K. The maximum loading at 760 mmHg at 283 K corresponds to an uptake of 8 wt%.

Photophysical studies

Pleasingly, both the free ligand and the strontium complex **1** exhibit the characteristic blue-green emission of the tetraarylpyrrolo[3,2-*b*]pyrrole fluorophore. This indicates that the non-conjugated spacer separating the coordinating group at the *N*-aryl position from the pyrrole core does indeed diminish the non-radiative decay pathways we observed in previous attempts to coordinate closed shell metal ions through this position. Although the ligand shows poor solubility in most solvents, a sufficient concentration could be achieved in DMSO to study the photophysical properties of this species. **H_4L1** displays a single absorption maximum at 397 nm in DMSO, with the corresponding emission band centred at 477 nm corresponding to a Stokes shift of 4230 cm^{-1}. The photoluminescence quantum yield of 0.69 is comparable to typical values observed for other unfused TAPP derivatives reported by Gryko and others.[22]

TAPP fluorophores are known to exhibit emission solvatochromism particularly when the *C*-aryl substituent contains a strongly electron withdrawing group (typically NO_2 or CN) in the *para* position, which in polar solvents can lead to symmetry breaking in the S_1 excited state from the centrosymmetric ground state.[23] Tang and co-workers have also detected AIE characteristics from TAPP carboxylate ligands,[24] suggesting both polarity and aggregation dependences on the emission characteristics of these species, which we have also observed to some extent in previous work with TAPP carboxylates.[15]

With this in mind, we first exposed solutions of **H_4L1** in DMSO to increasing quantities of water to test for any aggregation-induced emission enhancement. As shown in Fig. 8, molar ratios (χ_{DMSO}) from 100 : 0 to 3 : 97 DMSO : H_2O caused a complex series of changes in the emission spectra, broadening and decreasing the intensity of the original emission band (SI, Fig. S16) but also showing the partial growth of a higher energy band at λ_{em} = 457 nm. The new band showed a slight enhancement of emission intensity at χ_{DMSO} = 0.14 (SI, Fig. S16), but the total emission intensity remained significantly lower in the presence of any amount of H_2O compared to the pure DMSO solution, as visible to the eye under irradiation at 366 nm (Fig. 8). At very high loadings of H_2O, a similar green emission to the colour in pure DMSO is visible, likely due to aggregation of solid **H_4L1** in this solvent mixture (Fig. S15). These observations suggest that if an AIEE influence is in effect, it is weak compared to the quenching influence of water on the protonated species.

Introducing hydroxide ions simplified the photophysical behaviour, likely increasing solubility of the fluorophore in its anionic form(s) and potentially reducing the number of possible excited state intermolecular proton transfer pathways (at least those in which **H_4L1** could act as a donor). Adding small aliquots of 1 mM aqueous NaOH solution to a solution of **H_4L1** in DMSO showed gradual diminishing of the main emission band at 477 nm and growth of a comparable higher energy emission band at 445 nm with similar intensity, (SI, Fig. S18) likely corresponding to one or more **L1** anionic species. A solvent screen from pure DMSO to 1 mM $NaOH_{(aq)}$ was then performed (Fig. 9), where the emission band from the ligand in pure DMSO immediately converts to the fully deprotonated blue-emissive form from the first addition of NaOH. On further additions of aqueous hydroxide, this band then undergoes a red shift as the water content of the mixture increases. This observation is consistent with the species remaining soluble, with solvatochromism then following the expected trend towards a redder emission band simply based on the larger orientation polarizability of water compared to DMSO. Emission from the anionic form retains similar intensity up to much higher water fractions, and only diminishes in intensity at $\chi_{DMSO} < 0.2$.

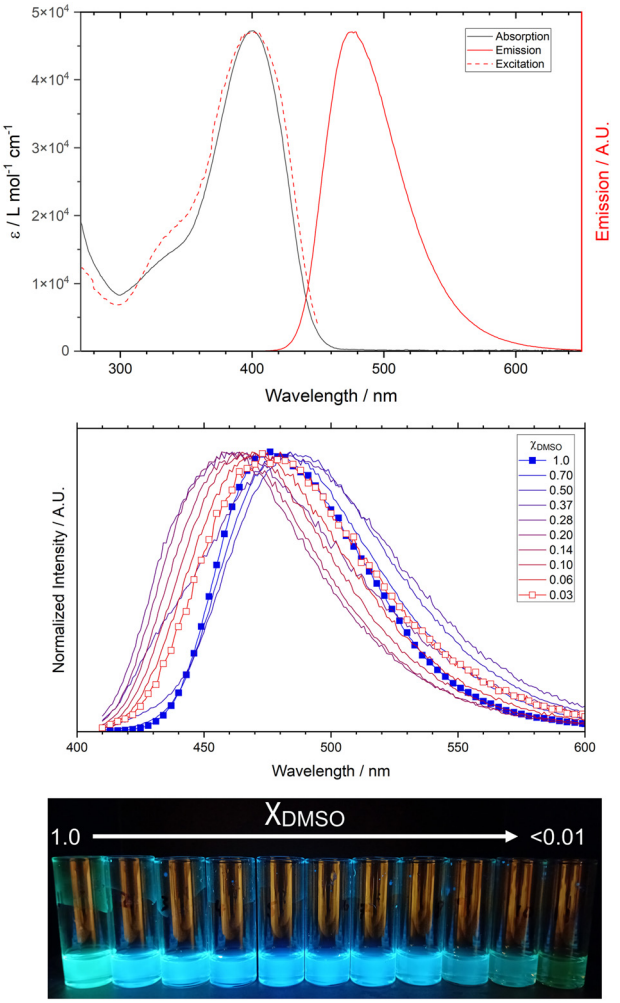

Fig. 8 (Top) Absorption, emission (λ_{ex} = 397 nm) and excitation (λ_{em} = 475 nm) spectra for **H_4L1** in DMSO (4.8 μM). (Middle) Emission spectra (λ_{ex} = 397 nm) for **H_4L1** in mixed solvent environments (4.3 μM) ranging from pure DMSO (filled blue squares, χ_{DMSO} = 1.0) to 97 : 3 H_2O : DMSO (hollow red squares, χ_{DMSO} = 0.03). (Bottom) Photograph of **H_4L1** solution dissolved (18 μM) in a series of DMSO : H_2O mixtures under UV irradiation (366 nm). The solvent compositions (L–R) match those in the spectra above, with the addition of χ_{DMSO} = 0.006 at the far right.

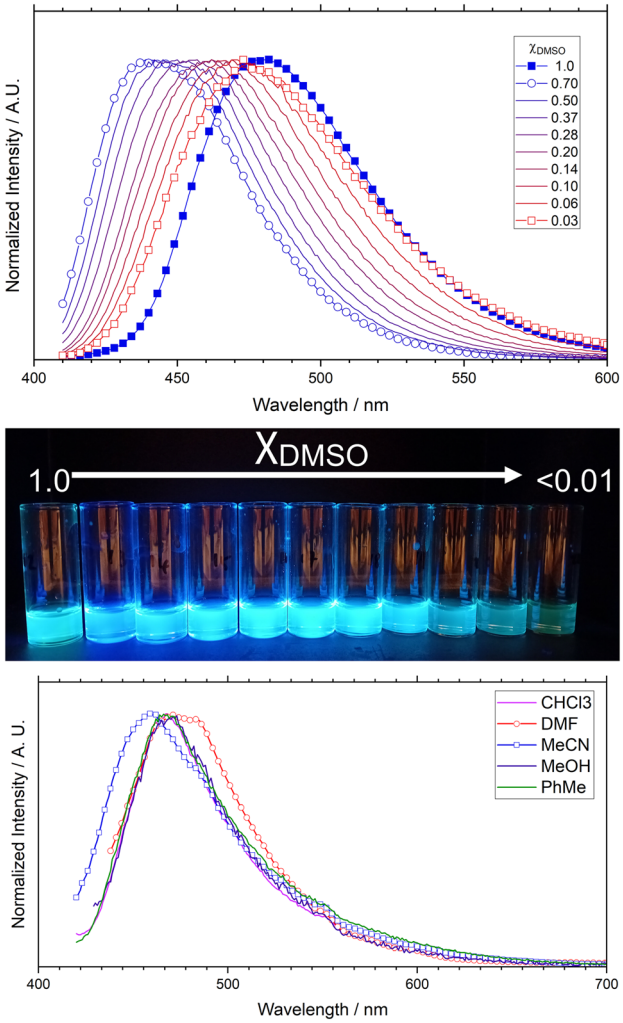

Fig. 9 (Top) Emission spectra (λ_{ex} = 397 nm) for H_4**L1** in mixed solvent environments (4.3 μM) ranging from pure DMSO (filled blue squares, χ_{DMSO} = 1.0) to 97 : 3 1 mM $NaOH_{(aq)}$: DMSO (hollow red squares, χ_{DMSO} = 0.03). The emission spectrum resulting from the first addition of NaOH is highlighted with hollow blue circles. (Middle) Photograph of H_4**L1** solution dissolved (18 μM) in a series of DMSO: 1 mM $NaOH_{(aq)}$ mixtures under UV irradiation (366 nm). The solvent compositions (L–R) match those in the spectra above, with the addition of χ_{DMSO} = 0.006 at the far right. (Bottom) Emission spectra (λ_{ex} = 404 nm) for the MOF **1** immersed in a series of solvents.

Given the *ca.* 1500 cm^{-1} spread of emission maxima between protonated and deprotonated forms of H_4**L1** as a function of DMSO : H_2O ratio, we examined the emission characteristics of the solid complex **1** to establish whether similar environment sensitivity was evident in the solid state. Crystalline samples of complex **1** were immersed in a range of solvents and the emission profile of the solids was tested at λ_{ex} = 404 nm. The pyrrolopyrrole fluorophore remained emissive on coordination to Sr^{2+} and following solvent exchange, with similar emission colour to the deprotonated form at high water fractions. As shown in Fig. 9, a small but detectable change in emission colour is seen between the pristine sample in DMF (λ_{em} = 472 nm) compared to the acetonitrile-soaked sample (λ_{em} = 461 nm). While the methanol, chloroform and toluene-soaked samples all show similar behaviour at an intermediate emission maximum (λ_{em} = 469 nm), the narrower peak shape compared to the pristine material is also consistent with a change to the fluorophore environment from incorporating these guests. Interestingly, the blue shift resulting from acetonitrile soaking compared to a redder emission from DMF is the opposite trend to that observed in our previous report of solvent exchange in a TAPP-based MOF. Acetonitrile having the larger orientation polarizability would lead to an expectation of a larger Stokes shift in solution. This suggests that while the behaviour of our previously reported (larger pore) system more closely relates to bulk solvent behaviour,[15] the much more confined pore environment in **1** may restrict solvent reorganization. While the fluorophore electronic environment and therefore excited state energetics are no doubt dominated by the immediately neighbouring groups and the nearby strontium cations, this solvent dependence indicates the fluorophore does remain somewhat sensitive to the occupancy of the channels.

Conclusions

In this study, we have shown incorporation of a methylene spacer between the coordinating carboxylate on the *N*-aryl substituent and a pyrrolo[3,2-*b*]pyrrole core provides a fluorescent tetratopic carboxylate ligand H_4**L1** which retains its emissive character upon coordination to a closed-shell metal ion. The structural tendencies of the TAPP core to assemble in the crystalline phase without close interactions between fluorophores is a promising route to MOFs and related microporous crystalline materials where small molecule guests may be able to access and influence the fluorophore environment directly. While the small pores in complex **1** evidently provided less opportunity for guests solvents to perturb the emission colour of the $L1^{4-}$ species, the encouraging level of solvatochromism shown by this anion in solution suggests that larger-pore MOFs with this ligand may pose a useful route towards responsive microporous materials.

Experimental

Synthesis of H_4L1

To a mixture of 4-aminophenylacetic acid (905 mg, 6.1 mmol) and *para*-toluenesulfonic acid monohydrate (110 mg, 0.65 mmol) in glacial acetic acid (5 mL) was added 4-formylbenzoic acid (900 mg, 6.0 mmol), and the resulting suspension was heated at 90 °C in air for 30 minutes. Following this period, 2,3-butanedione (260 μL, 2.99 mmol) was added dropwise over a 5 minute period, causing the thick suspension to loosen and turn dark brown. The suspension was stirred with heating continued for 3 hours, followed by cooling to room temperature. The solids were filtered, washed with 5 mL of glacial acetic acid and 2 × 10

mL methanol, and air dried. The filter cake was then suspended in 100 mL of boiling ethyl acetate and manually agitated to loosen the large particles, and hot filtered. The solids were further washed with ethyl acetate (2 × 50 mL) and methanol (2 × 50 mL), and air dried, to give a bright yellow powder. Yield 347 mg (0.57 mmol, 19%). m.p. >300 °C. δ_H (400 MHz, DMSO-d_6) 12.63 (br, 4H, H^1/H^8), 7.79 (d, 4H, J = 8.5 Hz, H^7), 7.31–7.36 (m, 8H, H^3/H^4), 7.25 (d, 4H, J = 8.5 Hz, H^6), 6.64 (s, 2H, H^5), 3.63 (s, 4H, H^2); δ_C (100 MHz, DMSO-d_6) 172.57, 167.05, 137.71, 137.04, 135.00, 133.12, 132.49, 130.60, 129.31, 128.17, 127.29, 124.78, 96.36, 40.09; ν_{max} (ATR, cm^{-1}) 2893m br, 2644w br, 2532w br, 1685s sh, 1598s, 1562w, 1516m, 1465m, 1410s, 1378m, 1269s, 1237m, 1185m sh, 1103m sh, 943m, 859s, 748s, 699s; m/z 613.1615 ($[M - H]^-$, calculated for $C_{36}H_{25}N_2O_8$ 613.1616); 306.0770 ($[M - 2H]^{2-}$, calculated for $C_{36}H_{24}N_2O_8$ 306.0772). λ_{max}/nm ($\varepsilon/10^3$ L mol^{-1} cm^{-1}) 397 (47.3); Φ_{PL} (±10%) 0.69.

Crystallisation of H_4L1·2DMF and H_4L1·4DMA

Single crystals of the title compounds were prepared by heating **H_4L1** (20 mg, 33 μmol) in either 2 : 1 DMF : H_2O (3 mL) or DMA (1 mL) at 100 °C in an 8 mL glass scintillation vial with a PTFE-lined cap for 16 hours. Single crystals for structural analysis were isolated directly from this solution, and bulk samples for X-ray powder diffraction were isolated by filtration of the mixtures. Masses of 3.4 mg and 9.6 mg were recovered for **H_4L1**·2DMF and **H_4L1**·4DMA respectively (14% and 30%, respectively).

Synthesis of poly-[Sr_2(L1)(DMF)$_2$(OH_2)]·DMF·H_2O 1

To a solid mixture of strontium nitrate tetrahydrate (9.3 mg, 33 μmol) and **H_4L1** (10 mg, 17 μmol) in an 8 mL Wheaton glass scintillation vial with PTFE-lined cap, was added 3 mL of a 2 : 1 DMF/water solution. The mixture was dispersed by sonication for 5 minutes, and then placed in a dry block heater and heated at 100 °C for 48 hours. The resulting orange crystals were isolated by hot filtration, washed with DMF (5 mL) and air dried. Yield 10.1 mg, 58%. m.p. >300 °C; ν_{max} (ATR, cm^{-1}) 3617w, 3360m br, 2925w, 1651m sh, 1601m, 1568s, 1540s, 1511s, 1453w, 1393s sh, 1280w, 1176m, 1136m, 1101s, 1013w, 936w, 851m, 818w, 793m, 756m, 737m, 710w, 667m; Found C, 48.75; H, 4.00; N, 5.27%; calculated for $C_{42}H_{48}N_4O_{16}Sr_2$ ([Sr_2(**L1**)(DMF)$_2$(OH_2)]·4(H_2O) C, 48.50; H, 4.65; N, 5.39%. The phase purity was confirmed using X-ray powder diffraction and compared to the simulated pattern from the single crystal X-ray dataset.

Author contributions

CLB, SHE: conceptualization, investigation, writing. SEW: investigation, supervision, formal analysis. CSH: conceptualization, investigation, supervision, formal analysis, writing.

Conflicts of interest

There are no conflicts to declare.

Data availability

Raw experimental data including unprocessed absorption and emission spectra, NMR and gas adsorption data are available from the Keele Data Repository at https://researchdata.keele.ac.uk/(DOI: https://doi.org/10.21252/jg25-6z02). Supplementary information (SI): general experimental and instrumental details, X-ray powder diffraction patterns and Rietveld refinement results, fingerprint plots, thermogravimetric analysis traces, further gas adsorption figures and details, additional fluorescence spectroscopy figures. See DOI: https://doi.org/10.1039/d5ce00926j.

CCDC 2488011–2488014 contain the supplementary crystallographic data for this paper.[25a–d]

Acknowledgements

The authors gratefully acknowledge the School of Chemical and Physical Sciences, Keele University for instrument funding support, Keele Central Sciences Laboratories for technical support, and CPS-WRITE for support with manuscript preparation. The authors gratefully acknowledge the Royal Society of Chemistry Research Grant for funding (RF18-5224).

Notes and references

1 (*a*) F.-X. Coudert, *Coord. Chem. Rev.*, 2025, **539**, 216760; (*b*) W. P. Lustig, S. Mukherjee, N. D. Rudd, A. V. Desai, J. Li and S. K. Ghosh, *Chem. Soc. Rev.*, 2017, **46**, 3242.

2 (*a*) J. Liu, T. A. Goetjen, Q. Wang, J. G. Knapp, M. C. Wasson, Y. Yang, Z. H. Syed, M. Delferro, J. M. Notestein, O. K. Farha and J. T. Hupp, *Chem. Soc. Rev.*, 2022, **51**, 1045; (*b*) G. A. Leith, C. R. Martin, J. M. Mayers, P. Kittikhunnatham, R. W. Larsen and N. B. Shustova, *Chem. Soc. Rev.*, 2021, **50**, 4382.

3 (*a*) S. Wang, B. Sun, Z. Su, G. Hong, X. Li, Y. Liu, Q. Pan and J. Sun, *Inorg. Chem. Front.*, 2022, **9**, 3259; (*b*) A. A. García-Valdivia, S. Pérez-Yáñez, J. A. García, B. Fernández, J. Cepeda and A. Rodríguez-Diéguez, *Sci. Rep.*, 2020, **10**, 8843.

4 (*a*) S. M. Moosavi, A. Nandy, K. M. Jablonka, D. Ongari, J. P. Janet, P. G. Boyd, Y. Lee, B. Smit and H. J. Kulik, *Nat. Commun.*, 2020, **11**, 4068; (*b*) O. G. Wood and C. S. Hawes, *CrystEngComm*, 2022, **24**, 8197.

5 (*a*) X. Wu, L. K. Macreadie and P. A. Gale, *Coord. Chem. Rev.*, 2021, **432**, 213708; (*b*) L. Esrafili, A. Morsali, M.-L. Hu, A. A. Tehrani, L. Carlucci, P. Mercandelli and D. M. Proserpio, *Inorg. Chem.*, 2020, **59**, 16421.

6 (*a*) N. B. Shustova, B. D. McCarthy and M. Dincă, *J. Am. Chem. Soc.*, 2011, **133**, 20126; (*b*) Z. Wei, Z.-Y. Gu, R. K. Arvapally, Y.-P. Chen, R. N. McDougald Jr., J. F. Ivy, A. A. Yakovenko, D. Feng, M. A. Omary and H.-C. Zhou, *J. Am. Chem. Soc.*, 2014, **136**, 8269.

7 (*a*) I. Del Castillo-Velilla, A. Sousaraei, I. Romero-Muñiz, C. Castillo-Blas, A. S. J. Méndez, F. E. Oropeza, V. A. de la Peña O'Shea, J. Cabanillas-González, A. Mavrandonakis and A. E. Platero-Prats, *Nat. Commun.*, 2023, **14**, 2506; (*b*) W. M. Bloch, A. Burgun, C. J. Doonan and C. J. Sumby, *Chem. Commun.*, 2015, **51**, 5486; (*c*) G. Ji, X. Gao, T. Zheng, W. Guan, H. Liu and Z. Liu, *Inorg. Chem.*, 2018, **57**, 10525.

8 (*a*) B. Gole, A. K. Bar and P. S. Mukherjee, *Chem. – Eur. J.*, 2014, **20**, 13321; (*b*) A. Tran, M. Leroux, C. Michelin, F. Réveret, D. Boyer and F. Cisnetti, *J. Mater. Chem. C*, 2023, **11**, 14896.

9 A. Sharma, D. Kim, J.-H. Park, S. Rakshit, J. Seong, G. H. Jeong, O.-H. Kwon and M. S. Lah, *Commun. Chem.*, 2019, **2**, 39.

10 S. G. Dunning, A. J. Nuñez, M. D. Moore, A. Steiner, V. M. Lynch, J. L. Sessler, B. J. Holliday and S. M. Humphrey, *Chem*, 2017, **2**, 579.

11 A. Janiga, E. Glodkowska-Mrowka, T. Stoklosa and D. T. Gryko, *Chem. – Asian J.*, 2013, **2**, 411.

12 D. H. Friese, A. Mikhaylov, M. Krzeszewski, Y. M. Poronik, A. Rebane, K. Ruud and D. T. Gryko, *Chem. – Eur. J.*, 2015, **21**, 18364.

13 (*a*) M. Tasior, P. Kowalczyk, M. Przybył, M. Czichy, P. Janasik, M. H. E. Bousquet, M. Łapkowski, M. Rammo, A. Rebane, D. Jacquemin and D. T. Gryko, *Chem. Sci.*, 2021, **12**, 15935; (*b*) M. Santra, Y. W. Jun, J. Bae, S. Sarkar, W. Choi, D. T. Gryko and K. H. Ahn, *Asian J. Org. Chem.*, 2017, **6**, 241.

14 (*a*) M. Krzeszewski, Ł. Dobrzycki, A. L. Sobolewski, M. K. Cyrański and D. T. Gryko, *Angew. Chem., Int. Ed.*, 2021, **60**, 14998; (*b*) M. B. Teimouri, I. Deperasińska, M. Rammo, M. Banasiewicz, C. W. Stark, Ł. Dobrzycki, M. K. Cyrański, A. Rebane and D. T. Gryko, *J. Org. Chem.*, 2024, **89**, 4657.

15 C. S. Hawes, G. M. Ó Máille, K. Byrne, W. Schmitt and T. Gunnlaugsson, *Dalton Trans.*, 2018, **47**, 10080.

16 (*a*) B. Zhao, Z. Yang, Z. Duan, Y. Liu, C. Yang, J. Duan, Y. Zhao and Z. Lin, *Cryst. Growth Des.*, 2024, **24**, 5447; (*b*) Y. Li, X. Li, S. Hia, C. Zhang, Y. Luo, Z. Lin, Y. Zhao and W. Huang, *Inorg. Chem.*, 2021, **60**, 12129; (*c*) C. Yang, Y. Liu, J. Li, S. Zhuang, F. Wang, Z. Lin, Y. Zhao and W. Huang, *Inorg. Chem.*, 2025, **64**, 5271; (*d*) L. Wang, W. Qiao, H. Liu, S. Li, J. Wu and H. Hou, *Inorg. Chem.*, 2023, **62**, 3817.

17 C. S. Hawes, K. Byrne, W. Schmitt and T. Gunnlaugsson, *Inorg. Chem.*, 2016, **55**, 11570.

18 P. C. Purba, S. Bhattacharyya, M. Maity, S. Mukhopadhyay, P. Howlader and P. S. Mukherjee, *Chem. Commun.*, 2019, **55**, 8309.

19 M. Krzeszewski, D. Gryko and D. T. Gryko, *Acc. Chem. Res.*, 2017, **50**, 2334.

20 S. S. Tan, S. J. Kim and E. T. Kool, *J. Am. Chem. Soc.*, 2011, **133**, 2664.

21 J.-B. Lin, T. T. T. Nguyen, R. Vaidhyanathan, J. Burner, J. M. Taylor, H. Durekova, F. Akhtar, R. K. Mah, O. Ghaffari-Nik, S. Marx, N. Fylstra, S. S. Iremonger, K. W. Dawson, P. Sarkar, P. Hovington, A. Rajendran, T. K. Woo and G. K. H. Shimizu, *Science*, 2021, **374**, 1464.

22 M. Tasior, O. Vakuliuk, D. Koga, B. Koszarna, K. Górski, M. Grzybowski, Ł. Kielesiński, M. Krzeszewski and D. T. Gryko, *J. Org. Chem.*, 2020, **85**, 13529.

23 B. Dereka, A. Rosspeintner, M. Krzeszewski, D. T. Gryko and E. Vauthey, *Angew. Chem., Int. Ed.*, 2016, **55**, 15624.

24 K. Li, Y. Liu, Y. Li, Q. Feng, H. Hou and B. Z. Tang, *Chem. Sci.*, 2017, **8**, 7258.

25 (*a*) CCDC 2488011: Experimental Crystal Structure Determination, 2025, DOI: 10.5517/ccdc.csd.cc2phzfm; (*b*) CCDC 2488012: Experimental Crystal Structure Determination, 2025, DOI: 10.5517/ccdc.csd.cc2phzgn; (*c*) CCDC 2488013: Experimental Crystal Structure Determination, 2025, DOI: 10.5517/ccdc.csd.cc2phzhp; (*d*) CCDC 2488014: Experimental Crystal Structure Determination, 2025, DOI: 10.5517/ccdc.csd.cc2phzjq.